

# Water Evaporation: A Transition Path Sampling Study

Patrick Varilly<sup>†,‡</sup> and David Chandler<sup>\*,†</sup>

*Department of Chemistry, University of California, Berkeley, California 94720, U.S.A.*

E-mail: [chandler@cchem.berkeley.edu](mailto:chandler@cchem.berkeley.edu)

---

\*To whom correspondence should be addressed

<sup>†</sup>University of California, Berkeley

<sup>‡</sup>Current address: Department of Chemistry, University of Cambridge, Lensfield Road, Cambridge CB2 1EW,  
UNITED KINGDOM

## Abstract

We use transition path sampling to study evaporation in the SPC/E model of liquid water. Based on thousands of evaporation trajectories, we characterize the members of the transition state ensemble (TSE), which exhibit a liquid-vapor interface with predominantly negative mean curvature at the site of evaporation. We also find that after evaporation is complete, the distributions of translational and angular momenta of the evaporated water are Maxwellian with a temperature equal to that of the liquid. To characterize the evaporation trajectories in their entirety, we find that it suffices to project them onto just two coordinates: the distance of the evaporating molecule to the instantaneous liquid-vapor interface, and the velocity of the water along the average interface normal. In this projected space, we find that the TSE is well-captured by a simple model of ballistic escape from a deep potential well, with no additional barrier to evaporation beyond the cohesive strength of the liquid. Equivalently, they are consistent with a near-unity probability for a water molecule impinging upon a liquid droplet to condense. These results agree with previous simulations and with some, but not all, recent experiments.

**Keywords:** Molecular dynamics, rare events, liquid-vapor interface, mean curvature, transition state ensemble, free energy profile

## Introduction

In a sample of water at equilibrium with its vapor, the rate of evaporation is equal to the rate of condensation. During condensation, not every gas molecule that impinges on a liquid surface necessarily sticks. The fraction that does stick is known as the *uptake coefficient*,  $\gamma$ , and by microscopic reversibility,  $\gamma$  can also be used to characterize evaporation.<sup>1</sup> Any deviation of  $\gamma$  from 1 signals some impediment to evaporation (or condensation) beyond the mere cohesive strength of the liquid. Measurements of  $\gamma$  have ranged from about 0.001 to 1 over the past century,<sup>2</sup> but over the last decade,<sup>3</sup> they have been converging to the range of 0.1 to 1. Li and coworkers<sup>4</sup> measured uptake of isotopically labeled water vapor in a train of water droplets to obtain  $\gamma = 0.17 \pm 0.03$  at 280 K, which increases with decreasing temperature. A similar result,  $\gamma = 0.15 \pm 0.01$  at 282.5 K, was obtained by Zientara and coworkers<sup>5</sup> from observations of freely evaporating water droplets levitated in an electrodynamic trap. Winkler and coworkers,<sup>6,7</sup> on the other hand, measured droplet growth in cloud chambers and claim to exclude values of  $\gamma < 0.4$  for temperatures below 290 K. Their data is, in fact, consistent with  $\gamma = 1$  for temperatures ranging from 250 K to 290 K. Experiments done in the Saykally and Cohen groups,<sup>3,8-10</sup> which measure the drop in temperature as water from a droplet in a droplet train evaporates into vacuum, indicate that  $\gamma = 0.62 \pm 0.09$  with little or no temperature dependence between 245 K and 298 K.

The experimental uncertainty makes it unclear whether or not there is a small barrier to evaporation. To address this uncertainty, we were motivated to carry out a detailed simulation study of evaporation using transition path sampling<sup>11</sup> (TPS), a rare-event sampling technique that can produce a statistically representative collection of short evaporation trajectories with Boltzmann-distributed (NVT) initial conditions and energy-conserving (NVE) dynamics. Roughly speaking, at 300 K, one water molecule evaporates from a  $1 \text{ nm}^2$  patch of a liquid-vapor interface every 10 ns, which motivates using a rare-event sampling technique. Other approaches could also be used to study evaporation. For example, in Ref. 12, a single long simulation of a small water droplet was performed at 350 K, resulting in 70 evaporation events. Another complementary approach is to study condensation probabilities, since condensation is not rare at all.<sup>13-15</sup> A full discussion of

the relationship between evaporation and condensation trajectories is given in the Appendix. The chief advantages of our approach are that we do not need to introduce the approximation that the velocities and angular momenta of the evaporated water molecule are Boltzmann-distributed, with a temperature equal to that of the liquid, and that we are able to generate a large number of evaporation trajectories (about 5000), which we can characterize statistically instead of anecdotally. Further, the framework for analyzing TPS simulations can be used to obtain novel insight into evaporation kinetics.

## Methods

Throughout, we run simulations of liquid water with LAMMPS<sup>16</sup> using the SPC/E model of water.<sup>17</sup> Lennard-Jones interactions are truncated and shifted at a distance of 10 Å. Electrostatic interactions are calculated using the particle-particle particle-mesh (PPPM) method,<sup>18</sup> with a relative error of  $10^{-4}$ . The bond and angle constraints of the water molecule are enforced using the SETTLE algorithm<sup>19</sup> to guarantee that trajectories are time-reversible. A timestep of 2 fs is used throughout. In simulations where we fix temperature, we use a Langevin thermostat with a time constant of 2 ps.

We use the SPC/E model of water because it adequately captures a broad swath of liquid water’s properties. With respect to bulk properties at 298 K, its radial distribution function is quite accurate,<sup>20</sup> its density is within 1% of experiment,<sup>21</sup> its compressibility<sup>22</sup> of  $4.1 \times 10^{-10} \text{ Pa}^{-1}$  is close to the experimental value of  $4.5 \times 10^{-10} \text{ Pa}^{-1}$ , and its dielectric constant<sup>23</sup> of 70 compares well with the experimental value of 78.2. The properties of its vapor-liquid transition are also quite good: the model is explicitly parametrized to reproduce the experimental enthalpy of vaporization,<sup>17</sup> its liquid-vapor surface tension is within about 10% of the experimental value,<sup>24–26</sup> and its vapor pressure is within a factor of 2 of the experimental value.<sup>27</sup> With regards to transport properties, its self-diffusion coefficient<sup>20</sup> of about  $2.8 \times 10^{-5} \text{ cm}^2/\text{s}$  compares well the experimentally measured value of  $2.3 \times 10^{-5} \text{ cm}^2/\text{s}$ . These properties lead us to believe that the SPC/E model cap-

tures sufficient water-like behavior to be useful in our study. The model is not polarizable, but its parametrization accounts implicitly for polarization in the bulk and results in a semiquantitatively correct description of the liquid-vapor interface. Of course, it is impossible to obtain arbitrarily precise quantitative agreement with experiments using SPC/E or any other classical model of water. However, the consistency of this model with general measures of liquid-vapor coexistence, interfacial energetics, and molecular fluctuation amplitudes and time scales gives us confidence in its qualitative predictions about the molecular dynamics of water evaporation.

Transition path sampling<sup>11</sup> is used to generate nearly 5000 independent evaporation trajectories of length 3 ps, which is long enough to avoid spurious biases (see Supplementary Information). Trajectories are constrained to start in a basin *A* in phase space, corresponding to a condensed state, and end in a basin *B*, corresponding to an evaporated state. In the analysis below, we consider only the trajectories for which the system enters basin *B* after at least 2 ps to avoid any biases towards unusually short evaporation trajectories.

Our explicit definitions of basins *A* and *B* are as follows. Basin *A* consists of all configurations where every water that is not hydrogen-bonded to any other water is at most 4 Å away from the nearest water (the “position of a water” means the position of its oxygen atom, unless otherwise stated). Following Ref. 28, two waters are considered hydrogen bonded if the distance between their oxygen atoms is below 3.5 Å and the angle between the OH bond of the donor and the line connecting the two oxygen atoms is below 30°. For our purposes, any other reasonable definition of a hydrogen bond should yield nearly identical results. Basin *B* is defined as all configurations of the system where there is exactly one water molecule with no hydrogen-bonding partner that is more than 8 Å away from its nearest neighbor. The distance cutoff used in defining basin *A* is motivated by the extremely low likelihood for a water in bulk to be that isolated. We comment on our choice for the cutoff for basin *B* below.

Transition path sampling is essentially a biased random walk in trajectory space. The initial trajectory of this walk is prepared as follows. We place water molecules in a crystalline arrangement in a  $30 \times 30 \times 30 \text{ \AA}^3$  periodic box so that the density of water molecules matches the bulk density of

water (33.3 waters per  $\text{nm}^3$ , equivalent to 0.997 g/ml), i.e., 900 waters in total, and equilibrate this system at 300 K for 50 ps. Next, we enlarge the box to three times its size along the  $z$ -dimension, and equilibrate the resulting system for another 50 ps. At this stage, we have a  $30 \times 30 \times 90 \text{ \AA}^3$  periodic box containing a  $30 \text{ \AA}$ -thick slab of water parallel to the  $xy$ -plane. We then add a water molecule about  $15 \text{ \AA}$  above the top of this slab with a random, thermal velocity. An example of the system at this stage is shown in Figure 1. Next, we evolve the system without a thermostat to yield a 3 to 9 ps-long trajectory. If in this time, the water molecule does not condense (i.e., enter basin A), we discard this initial trajectory and start over. Otherwise, we time-reverse the 3 ps stretch of the trajectory immediately preceding condensation, and use this reversed evaporation trajectory to seed the TPS random walk. We have verified that condensation fails to occur about 50% of the time, and that in all cases is due to the water molecule having initial total momentum with a positive  $z$ -component, so that the molecule moves away from the water slab during the trajectory. We have not observed any initial trajectory with a water molecule initially headed towards the water slab and not condensing, a fact that is consistent with a sticking coefficient  $\gamma$  of nearly 1, as observed in previous similar simulations.<sup>13–15</sup>

The TPS random walk is performed as follows. At every step, we choose to make a shifting move 90% of the time, and a shooting move 10% of the time, reflecting the low cost of shifting versus shooting. In a shifting move, we shift the trajectory forwards or backwards by a time  $\Delta t$  uniformly distributed between  $-1$  and  $1$  ps. Shooting moves are performed as in the appendices of Refs. 29 and 30. Briefly, the  $3N$ -dimensional vector of velocities weighted by the square root of the atomic masses is rotated slightly, then projected down to a hyperplane to enforce the constraints on velocities imposed by the fixed bonds and angles of the water molecules. The kinetic energy of the system is then perturbed slightly. Generation and acceptance probabilities for this move are chosen to satisfy detailed balance, and the magnitude of the perturbations is chosen to yield an approximately 40% acceptance rate.

For each set of initial conditions, we performed between 10,000 and 20,000 TPS steps, recording a trajectory every 100 TPS steps. Each recorded trajectory is reasonably independent of the

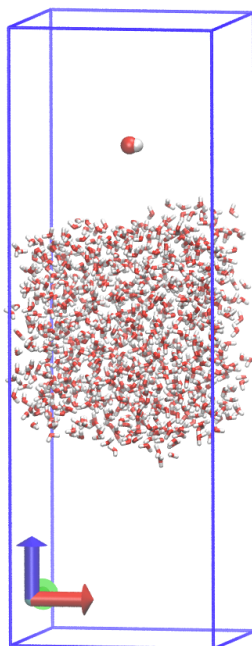


Figure 1: Snapshot of setup used to study water evaporation.

previous one, and the first 20 recorded trajectories, which form the equilibration part of the random walk, are discarded. To further improve the sampling, we repeated the entire procedure outlined in this section about 40 times. The final outcome of this exercise is a set of 4696 mostly uncorrelated evaporation trajectories, with initial conditions drawn from a canonical ensemble at temperature 300 K and evolved in time with energy-conserving Newtonian dynamics.

Our procedure induces a bias for evaporation trajectories where a single water molecule comes off the liquid. This bias arises from our definition of basin  $B$  for the TPS random walk. Before settling on this definition, we explored the possibility of events where dimers or larger aggregates of water evaporate as a unit, by using a more generous but cumbersome definition of basin  $B$ . Specifically, a configuration was in basin  $B$  if it contained exactly two separate clusters of waters, in each of which every water was close to some other water in the cluster. By observing the evaporation events in these preliminary simulations, we convinced ourselves that out of the rare events in which evaporation occurs, those involving more than one water were far rarer still, so we

neglected this possibility in our final simulations in favor of using a simpler definition of basin  $B$ .

In analyzing the evaporation trajectories, it is useful to locate the liquid-vapor interface at any instant in time, for which we use the method of Ref. 31. Briefly, we map a given configuration of water oxygen atoms  $\{\mathbf{r}_i\}$  onto a smooth density field  $\tilde{\rho}(\mathbf{r})$  defined by the relation

$$\tilde{\rho}(\mathbf{r}) = \sum_{i=1}^N \phi(|\mathbf{r} - \mathbf{r}_i|), \quad (1)$$

where  $N$  is the number of water molecules, and  $\phi(r)$  is a Gaussian-like smoothing function of width  $\xi = 2.5 \text{ \AA}$  (see Appendix). The instantaneous liquid-vapor interface is then defined implicitly as the set of points  $\{\mathbf{s}\}$  that satisfy

$$\tilde{\rho}(\mathbf{s}) = (1/2)\rho_\ell, \quad (2)$$

where  $\rho_\ell$  is the bulk density of liquid water.

After locating the liquid-vapor interface, we follow Ref. 31 in defining a perpendicular distance  $a$  from a probe water molecule at  $\mathbf{r}$  to the interface, as illustrated in Figure 2. First, we locate the point  $\mathbf{s}$  on the interface closest to  $\mathbf{r}$ , and calculate the vapor-pointing normal vector to the interface there,  $\hat{\mathbf{n}}$ . Then  $a$  is defined as the distance from  $\mathbf{r}$  to  $\mathbf{s}$  projected along the  $\hat{\mathbf{n}}$  direction,

$$a = \hat{\mathbf{n}} \cdot (\mathbf{r} - \mathbf{s}). \quad (3)$$

In Ref. 31, this distance was denoted by  $a^*$ .

An ambiguity arises about whether the probe molecule at  $\mathbf{r}$  should or should not be included when calculating the position of the liquid-vapor interface. Generally, we exclude it when calculating  $a$ . To discuss the consequences of this choice, we define  $a'$  analogously to  $a$ , but with the probe water molecule included in the definition of the liquid-vapor interface.





Figure 2: Definition of water-to-surface distance  $a$  (or  $a'$ ). The plane shown is the tangent plane to the liquid-vapor interface at the point closest to the probe water molecule. In (a), the probe water is excluded from the definition of the interface; in (b), it is included. These snapshots illustrate a typical interfacial deformation that accompanies an evaporation event. The system is depicted at its transition state.

## Results

### Evaporation correlates with negative mean curvature

We first focus on the molecular details of the transition states of the evaporation trajectories. Ordinarily,<sup>11</sup> transition states are identified using committor functions. The committor,  $p_B(\mathbf{x})$ , of a spatial configuration  $\mathbf{x}$  is defined as the fraction of short trajectories that start at  $\mathbf{x}$  with random thermal velocities, and finish in basin  $B$ . At most points in a transition path, this function is either 0 or 1, with a quick crossover around the configurations that dominate the dynamical bottleneck between  $A$  and  $B$ . Thus, a pragmatic definition of a transition state along a trajectory is the point where  $p_B(\mathbf{x}) = 0.5$ .

Implicit in the above definition of the committor function is the assumption that momenta are not important in characterizing transition states. In a dense system, this assumption is generally true, since the velocity of any particle decorrelates rapidly, usually within 1 ps.<sup>32</sup> When examining evaporation, the assumption breaks down, since the velocity of an evaporated water molecule decorrelates over much longer timescales. The clearest manifestation of the problem is that the standard definition of  $p_B(t)$  leads to  $p_B(t) \approx 0.5$  for a configuration containing a single, clearly

evaporated water molecule, since the water can likely recondense if its rethermalized velocity points towards the liquid slab.

As a compromise, we have chosen to redefine the committor function to include the  $z$ -component of the velocity of the evaporated water molecule. Strictly speaking, it’s impossible to tell which water molecule is “the evaporated molecule” in an *arbitrary* configuration, but this is not a problem for identifying transition states along a transition path. Figure 3 illustrates the typical behavior of  $p_B(t) = p_B(\mathbf{x}(t), v_z^{\text{evap}}(t))$  defined in this way, estimated by spawning 10 short trajectories at every time point.

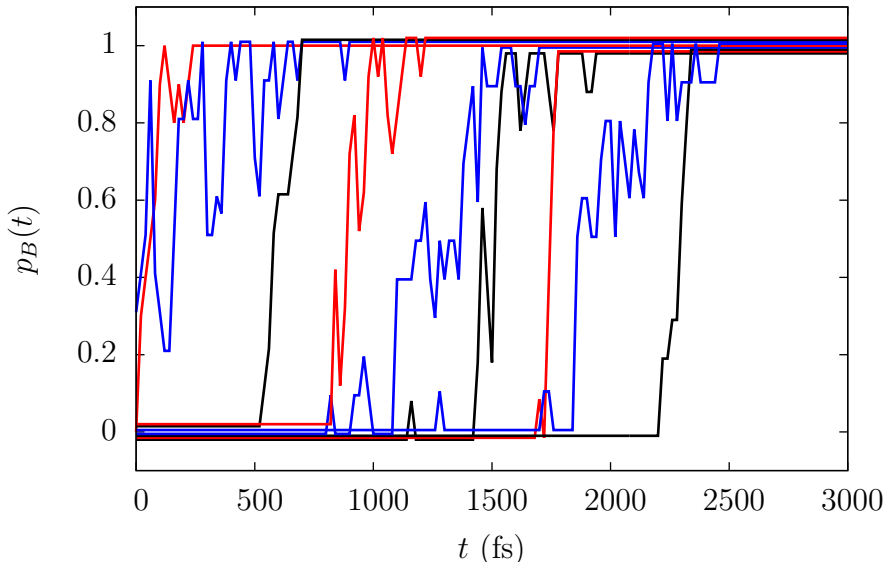


Figure 3: Estimated committor,  $p_B(t)$ , sampled at 20fs intervals for several evaporation trajectories. The error in  $p_B$  in the region around 0.5 is about 0.15. To obtain this estimate, all velocities but the  $z$ -component of the evaporated water’s velocity are randomized independently 10 times, after which a short trajectory is evolved forwards in time for up to 5ps until the systems enters either basin  $A$  or basin  $B$ . For clarity, individual committors are slightly displaced vertically.

We have defined the transition states as the configuration at a time  $t_c$  equal to the mean of the first time for which  $p_B(t)$  exceeds 0.4 and the first time for which it exceeds 0.6. The exact value of  $t_c$  is not very sensitive to the chosen cutoffs, as long as they are reasonable. The set of all configurations of the evaporation trajectories at their respective times  $t_c$  comprises the transition state ensemble (TSE).

In many condensed-phase phenomena, collective coordinates are key. Positions of individual atoms in the TSE do not by themselves appear particularly remarkable or extraordinary. Visual inspection confirms this state of affairs in this particular case. Instead, it is essential to characterize the members of the TSE by looking for statistical trends in a few collective coordinates. Here, we focus on the instantaneous liquid-vapor surface. Let  $\mathbf{s}$  be the point on this surface that is closest to the evaporating water molecule at any given time. The mean curvature,  $H$ , of the surface at  $\mathbf{s}$  serves as a concise characterization of collective fluctuations of water molecules at the liquid-vapor surface. The mean curvature is defined as<sup>33</sup>

$$H = \frac{k_1 + k_2}{2}, \quad (4)$$

where  $k_1$  and  $k_2$  are the principal curvatures at  $\mathbf{s}$ . The magnitude of a principal curvature is the reciprocals of the principal radius of curvature, and its sign specifies whether the surface curves towards (positive) or away (negative) from the normal direction along the corresponding principal direction. The mean curvature characterizes the change in surface area upon infinitesimal deformation of the surface, so it can be interpreted as a local characterization of the force of surface tension on the liquid-vapor surface. In particular, a deformation along the normal direction by an infinitesimal distance  $\varepsilon$  changes the area element  $dA$  as<sup>33</sup>

$$dA \mapsto (1 - 2\varepsilon H)dA. \quad (5)$$

To establish a baseline, we first calculate the distribution of  $H$  as a function of the height  $a$  of a probe water molecule from the liquid-vapor interface. Figure 4 shows the results as a joint free energy for  $H$  and  $a$  (respectively,  $H'$  and  $a'$  if the probe water molecule is included in the definition of the liquid-vapor interface), calculated using umbrella sampling as described in the Appendix. At very low and very high  $a$ , only a trivial bias in  $H$  is seen as a function of  $a$ , resulting from the nearest point on the surface being preferentially one where the surface is bending most towards the probe water molecule. However, an evident additional bias towards negative mean curvature can

be seen for  $a$  just above the surface, indicating that a water molecule suspended there significantly deforms the surface below it. Figure 2 shows an example of this kind of deformation in one of the harvested evaporation trajectories.

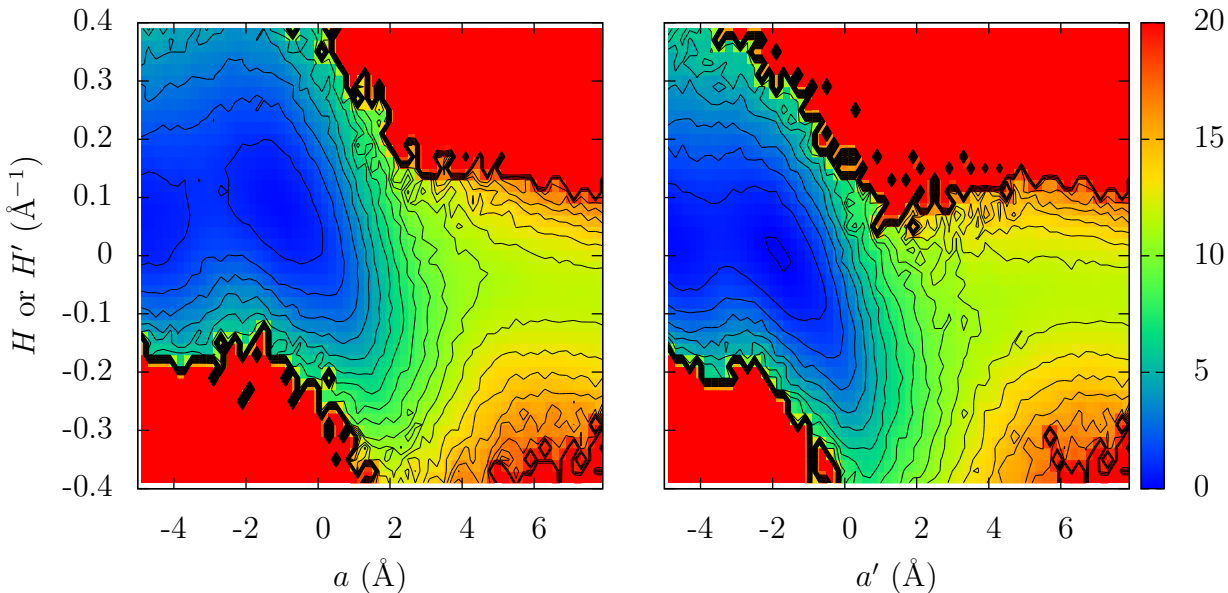


Figure 4: Free energy for height  $a$  of a probe water molecule and the mean curvature,  $H$ , at the nearest point on the liquid-vapor surface (respectively  $a'$  and  $H'$  if the probe water molecule is included in the definition of this surface). Contours are spaced at  $1 k_B T$ .

Figure 5 overlays the transition states of the evaporation trajectories on the free energies of Figure 4. To a certain extent, the transition states exhibit some of the bias towards negative curvature that can be seen in the equilibrium free energies. The bias is slight when the probe molecule is not included in the definition of the liquid-vapor surface, but is clearer when the probe molecule is included. The definition of a liquid-vapor interface during the evaporation process is somewhat ambiguous, and we regard full inclusion and full exclusion as the two limiting extremes for a suitable definition. Since the bias towards negative curvature is present in both cases, our finding should be robust with respect to reasonable changes in the definition of the interface.

As discussed below, the preponderance of negative-mean-curvature liquid-vapor interfaces

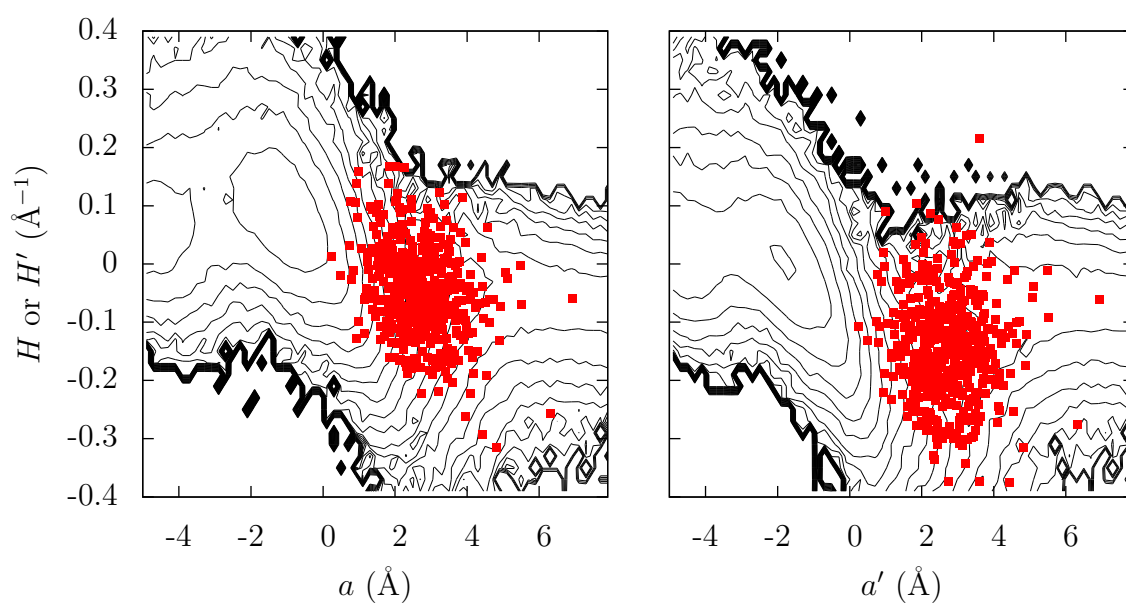


Figure 5: Representative transition states of evaporation trajectories (red) projected onto the  $H$  and  $a$  coordinates. The free energies of these coordinates are shown for comparison. Labels as in Figure 4.

does not correspond to an entropic barrier to evaporation, but instead is a molecular manifestation of the cohesive strength of the liquid. Nevertheless, we anticipate that external influences might be used to alter the microscopic details we describe, and so may perhaps be used to exert control over evaporation. Additionally, our characterization establishes a baseline for understanding evaporation under different conditions where barriers *are* observed in simulations, such as at higher temperatures<sup>13</sup> or in the presence of surfactants.<sup>34</sup>

## Post-evaporation momenta are Boltzmann-distributed

We now examine the center-of-mass velocities and angular momenta at the end of each trajectory. In all of the following results, we first estimate the value of each observable independently in each TPS run, and then report the mean of these values, with an error bar estimated as the standard error of the mean.

Figure 6(a) shows the distributions of the component of the evaporated water molecule’s center-of-mass velocity along a direction perpendicular to  $\hat{\mathbf{z}}$ , measured at the end of an evaporation trajectory. Figure 6(b) shows the analogous distribution of the components of angular momenta along the principal axes of inertia of the evaporating water molecule. Both sets of distributions are consistent with Boltzmann statistics at temperature  $T = 300$  K.

The component of the velocity along the  $z$  direction,  $v_z$ , has a more interesting distribution, shown in Figure 6(c). We enforce the constraint that water molecules first enter basin  $B$  with a positive  $v_z$  by flipping trajectories where this is not the case. Hence, no water molecules should have negative  $v_z$  at the end of the evaporation trajectory if the definition of basin  $B$  were sufficiently strict. In practice, the definition of basin  $B$  used here does not perfectly discriminate between the evaporated states and states where recondensation will occur. Since the trajectories examined here are finite, a trajectory where the system that transiently enters  $B$  before recondensing may appear as an evaporation event, but with  $v_z < 0$  at the end of the trajectory. Only about 1% of our trajectories exhibit this problem, which can in principle be mitigated by using longer trajectories and a stricter definition of basin  $B$ .

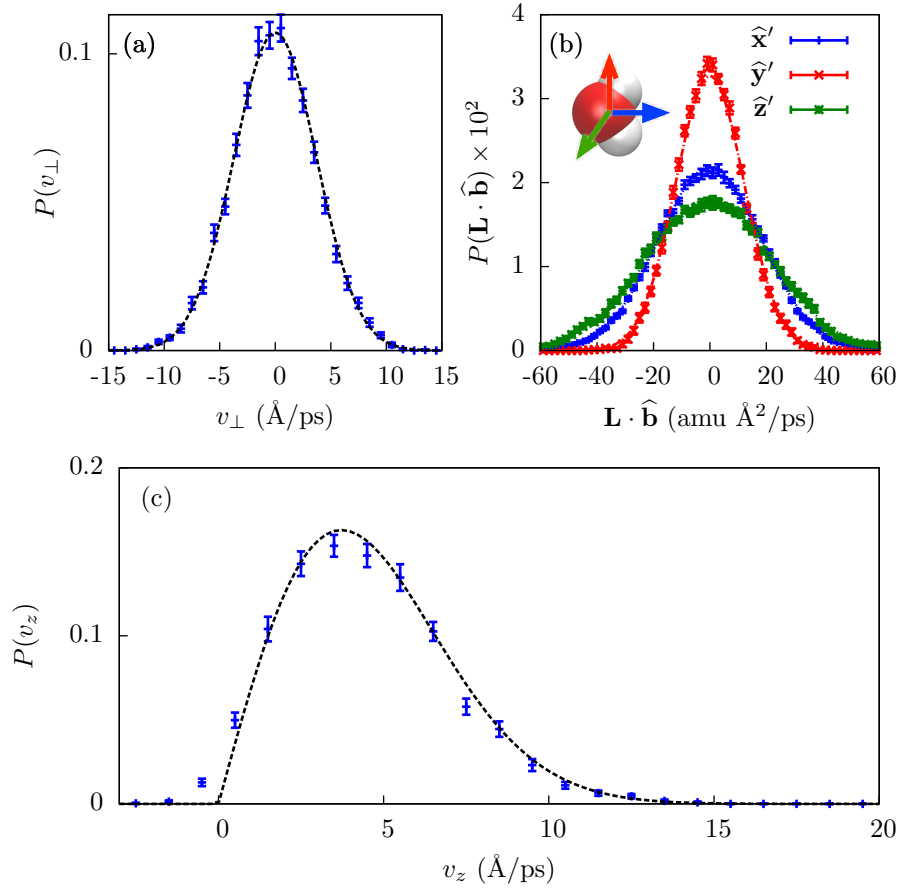


Figure 6: Distribution of (a) the component of center-of-mass velocity perpendicular to  $\hat{\mathbf{z}}$ ; (b) the components of angular momentum of the evaporated water along the principal axes of inertia, measured at the end of an evaporation trajectory (symbols); and (c) the  $z$ -component of center-of-mass velocity. For (a) and (b), the relevant Boltzmann distributions at temperature  $T = 300\text{ K}$  are also shown (dashed lines). For (c), the expected result for thermal ideal gas particles evaporating from a deep, barrierless potential well is shown (Equation (10), dashed line).

The expected distribution of  $v_z$  for positive  $v_z$  can be deduced from a simple model (Figure 7) of thermal ideal gas particles evaporating from a deep, barrierless potential well of depth  $\Delta U$ . Particles inside the well have a thermal distribution of velocities,  $P(v_i)$ , given by

$$P(v_i) \propto \exp\left(-\frac{1}{2}\beta m v_i^2\right). \quad (6)$$

A particle with initial velocity  $v_i$  can only escape the well if  $v_i$  is above a threshold velocity,  $v_t$ , given by  $\frac{1}{2}m v_t^2 = \Delta U$ . Were there a barrier, this threshold velocity would be higher, but the remainder of this discussion would carry through unchanged. The final velocity of this particle,  $v_f$ , is determined by conservation of energy, independent of the details of any intermediate barrier:

$$\frac{1}{2}m v_i^2 = \frac{1}{2}m v_f^2 + \Delta U. \quad (7)$$

This equation relates the distributions of initial and final velocities,  $P(v_i)$  and  $P(v_f)$  respectively, after correcting for the fact that for finite trajectories, high initial velocities are overrepresented by a factor of  $|v_i|$ , as there are proportionally more possible starting positions compatible with the particle being outside the well at the end of the trajectory. The exact relationship is

$$P(v_f)dv_f \propto P(v_i)|v_i|dv_i, \quad (8)$$

so

$$P(v_f) \propto P(v_i)|v_i| \frac{dv_i}{dv_f} \propto \exp\left(-\frac{1}{2}\beta m v_i^2\right) \frac{|v_i| \cdot v_f}{\sqrt{v_f^2 + \frac{2\Delta U}{m}}}. \quad (9)$$

Since the denominator in the last fraction is equal to  $|v_i|$ , we have

$$P(v_f) = \begin{cases} \frac{m}{k_B T} v_f \exp\left(-\frac{1}{2}\beta m v_f^2\right), & v_f > 0, \\ 0, & v_f \leq 0. \end{cases} \quad (10)$$

Were there a barrier of height  $B$  to evaporation, the threshold  $v_f$  above would be  $\sqrt{2B/m}$  instead



of 0, but the functional form would remain unchanged.

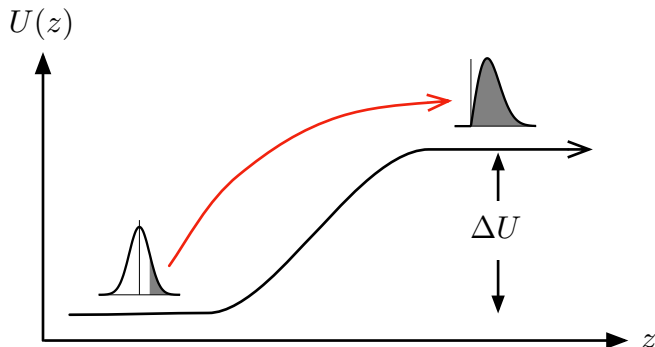


Figure 7: Ideal gas particles at the bottom of a deep, barrierless potential well have a Boltzmann distribution of velocities. Only a fraction of particles have enough energy to escape the well. After evaporating, but before thermalizing outside the well, the distribution of velocities of these particles is given by Equation (10).

While Equation (10) was derived for an ideal gas of thermal particles escaping from a deep, barrierless potential well, it also follows more generally from considerations of time reversibility (see Appendix) and it describes the observed distribution of  $v_z$  for evaporating molecules surprisingly well (dashed line in Figure 6(c)). In particular, low-velocity particles are not underrepresented, which is consistent with there being no barrier to evaporation. A similar velocity distribution has been reported in simulations of argon evaporation, which can be observed straightforwardly without special sampling techniques like TPS.<sup>13</sup>

## Potential of mean force for removing a water molecule from bulk is barrierless

Figure 8 shows the free energy,  $F(a)$ , of an arbitrary water molecule in our system as a function of the perpendicular distance to the instantaneous liquid-vapor interface  $a$ , calculated using umbrella sampling (see Appendix). Such a free energy profile is a reversible work or a potential of mean force surface (i.e., its negative gradient is equal to the mean force experienced by a water molecule along the  $a$  coordinate<sup>32</sup>). The essential feature of this free energy is that it is barrierless. Apart from density layering in the bulk,<sup>31</sup> manifested as oscillations in  $F(a)$  for  $a \lesssim 0 \text{ \AA}$ , the bulk liquid

simply sets up a deep potential well for any individual water molecule, and a molecule in the vapor can simply roll downhill into this well. While the absence of a barrier along the  $a$  coordinate does not preclude the existence of barriers along other coordinates, we demonstrate below that the transition states of the evaporation trajectories are consistent with  $a$  describing the majority of the evaporation reaction coordinate.

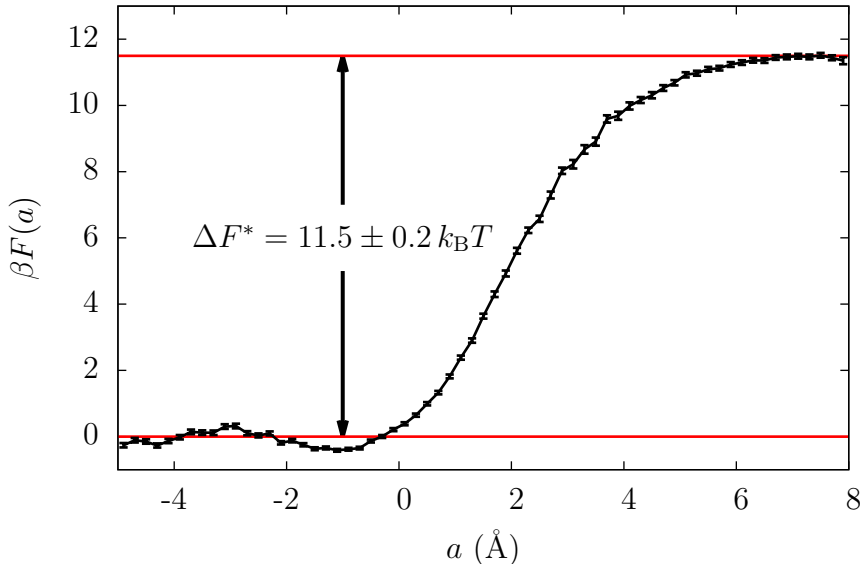


Figure 8: Free energy for a single water molecule at a perpendicular height  $a$  from the liquid-vapor interface defined by the remaining water molecules. The red lines are the free energies of the stable liquid and vapor phases, and are guides to the eye. The biasing potentials used extend to  $a = 7 \text{ \AA}$ , so the apparent downturn at  $a = 8 \text{ \AA}$  is not statistically significant.

The depth of the well in  $F(a)$ , denoted by  $\Delta F^*$ , quantifies the cohesiveness of the liquid with respect to the vapor. Indeed, if we regard a single water molecule as an independent particle moving in the potential well  $F(a)$ , then the relative density of this particle in the liquid,  $\rho_\ell$ , with respect to that in the vapor,  $\rho_g$ , is given by

$$\rho_g = \rho_\ell e^{-\beta \Delta F^*}. \quad (11)$$

We estimate from Figure 8 a value of  $\Delta F^*$  of  $11.5 \pm 0.2 k_B T$ . This compares favorably with the value of  $11.8 k_B T$  obtained by setting  $\rho_g = P_{\text{vap}}/k_B T$  and using the computed value of  $P_{\text{vap}}$  for

SPC/E water at a temperature of 300 K and pressure of 1 atm.<sup>27</sup> For real water, the analogous calculation yields  $\Delta F^* = 10.5 k_B T$ .

The range of  $F(a)$  also characterizes the effective range of attraction between a molecule in the vapor and the bulk slab, just under 8 Å. It is this range that motivates the definition of basin  $B$  described in the Methods section. Different models of water will have slightly different ranges of attraction, but we do not expect discrepancies in the qualitative behavior of  $F(a)$ .

Others have calculated a similar potential of mean force, but with respect to the distance from the Gibbs dividing surface instead of the instantaneous liquid surface, so that the details of the potential are masked by the capillary wave fluctuations of the liquid-vapor interface. Nevertheless, their results for the SPC/E water model<sup>35</sup> and for a polarizable water model due to Dang and Chang<sup>36</sup> are broadly similar to each other and to our own results.

### Transition states are consistent with diffusion out of a deep well

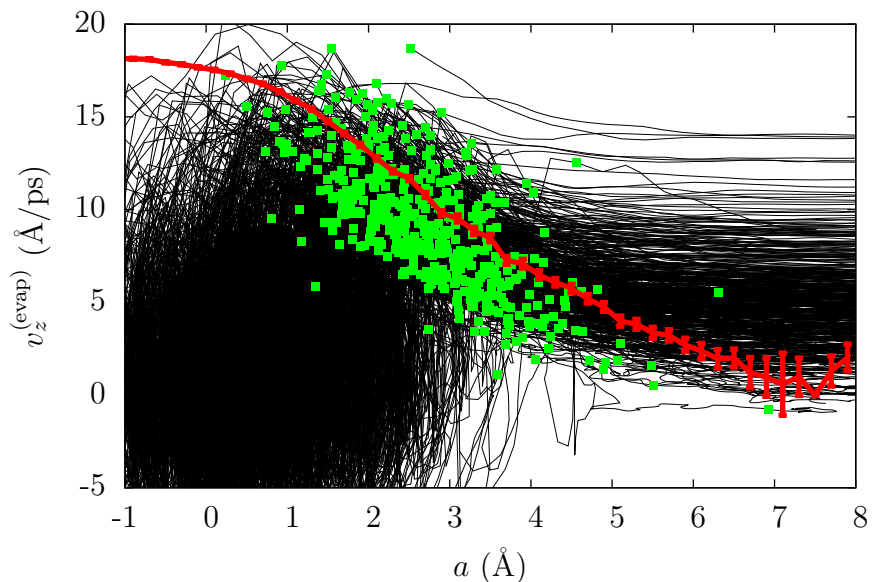


Figure 9: Evaporation trajectory traces projected onto variables  $v_z^{(\text{evap})}$  and  $a$  (black lines). The transition state of each trajectory, identified as described in the text, is highlighted by a green dot. Red line: the expected transition state ensemble for a coarse model of ballistic escape from a potential shaped as in Figure 8, given by Equation (12).

Figure 9 depicts traces of many evaporation trajectories projected onto the two coordinates  $v_z^{(\text{evap})}$  and  $a$ , with the transition state of each trajectory highlighted in green. Unlike similar traces onto many other pairs of coordinates (not shown), there is a definite correlation between the distance of the evaporated water from the liquid-vapor interface and its speed in the  $z$  direction. We can partially rationalize this dependence by conceiving of the free energy along  $a$  (Figure 8) as an actual potential energy well, and approximating the velocity along the  $a$  direction with  $v_z^{(\text{evap})}$ . If evaporation were a ballistic escape from this well, then the transition states would satisfy the condition

$$\frac{1}{2}m(v_z^{(\text{evap})})^2 = F(a). \quad (12)$$

The points satisfying this relation are shown as a thick red line in Figure 9. Despite the evident crudeness of the model, the transition states clearly cluster around the line of Eq. (12).

## Discussion

We have examined the process of evaporation of SPC/E water in detail, and all the evidence suggests that there is no barrier to evaporation in this model. In other words, to evaporate, a water molecule near the surface only needs to spontaneously acquire enough kinetic energy in the direction of the liquid-vapor interface normal. This view is consistent with the distribution of  $v_z$  for the final velocities (Figure 6(c)), the fact that the potential of mean force along a coordinate  $a$  perpendicular to the liquid-vapor surface is barrierless (Figure 8) and the fact that the transition states cluster around values of  $v_z$  and  $a$  that have a threshold amount of energy to escape from the potential well set up by the remainder of the bulk (Figure 9). It is difficult to imagine evaporation to be a mildly activated process and still be consistent with these three pieces of evidence.

Our results are consistent with the near-unit condensation coefficient measured in simulations in Refs. 13, 14 and 15, but is in apparent contradiction with the most recent experimental results,<sup>3,8-10</sup> which suggest a barrier of around  $-k_B T \ln(\gamma) \approx 0.5 k_B T$ . The other experimental results cited in the introduction suggest anything from the absence of a barrier to a barrier of up

to  $1.9k_{\text{B}}T$ . Excluding the possibility that water molecules evaporate as dimers, which would imply that an appreciable fraction of water molecules in the vapor are dimerized (and recall that our preliminary transition path sampling showed that there is not a significant fraction of SPC/E water molecules that evaporate or condense as dimers or as larger clusters), such large barriers should be clearly evident in direct simulations of water condensation, but they are conspicuously absent.<sup>13,15</sup>

The general lack of consensus between experiments<sup>3-7</sup> makes it unclear whether or not our result of apparent unit evaporation coefficient agrees with reality, or if it is an artifact of our simulations. In particular, it could be that there is indeed a barrier to evaporation and we cannot capture it, if that barrier were due to fundamentally quantum effects. By construction, these effects are beyond the scope of the classical molecular dynamics simulations used here. Important quantum effects are plausible because librational motions of water are strongly quantized: their typical wavenumbers, around  $500\text{cm}^{-1}$ , are comparable to the thermal wavenumber at  $T = 300\text{K}$ , around  $200\text{cm}^{-1}$ . More sophisticated simulation techniques can incorporate many quantum effects at reasonable cost. A notable exception would be dynamical quantum coherence,<sup>37</sup> for which a significant role would be surprising for intermolecular motions in a strongly dissipating system like liquid water. If quantum effects were limited to quantum dispersion and simple tunneling behavior, for instance, one could explore the consequences of quantum uncertainty using ring-polymer molecular dynamics.<sup>38</sup> However, our firm expectation is that these more sophisticated simulations will produce results that agree with those presented here, since generally, tunneling and dispersion tend to lower effective barriers with respect to classical expectations, not increase them. Moreover, any account of such quantum effects playing a dominant role would have to be compatible with the observation<sup>9</sup> that the evaporation coefficient of  $\text{D}_2\text{O}$  is equal, within errors, to that of  $\text{H}_2\text{O}$ .

Another possible source of discrepancy is our use of the SPC/E model of water, and in particular, its lack of polarizability, which might result in a qualitatively inaccurate description of events at the liquid-vapor interface. However, the agreement of its surface tension to the experimental value (within about 10%) suggests that the SPC/E model's parameters implicitly capture enough detail about polarization to describe the general mechanistic behavior of the liquid-vapor interface.

Moreover, the addition of polarizability would likely reduce, not enhance, any barriers to evaporation and/or condensation, since polarization induces an additional attractive force between the liquid and a vapor molecule that is relatively long-ranged. Significantly, a previous study of direct condensation that used the POL3 model of water,<sup>15</sup> which is polarizable, is consistent with  $\gamma \approx 1$ , i.e., barrierless evaporation.

Finally, extracting the evaporation coefficient from experiments involves some interpretation and extrapolation, so it is conceivable that the quoted results may be skewed by systematic errors that have not been accounted for. For example, Morita et al.<sup>14</sup> have previously argued that Li et al.'s low reported evaporation coefficient<sup>4</sup> may actually be compatible with a value in the range of 0.2 to 1 once the effects of fluid flow on the gas surrounding their water droplet train are corrected for. As for the more recent experiments of Refs. 3, 8, 9 and 10, these rely on a linear extrapolation of van't Hoff behavior of the Raman spectrum of water down to supercooled temperatures in order to measure the temperature of evaporating water droplets. Recent Raman spectra of magnetically trapped supercooled droplets, however, show that this extrapolation may not be accurate.<sup>39</sup> This suggests that the observed deviation from unit evaporation coefficient may also be in part due to shortcomings in the calibration step of the experiments. A systematic error of 2% in absolute temperature in the experiments (equal to about 10% in the temperature change during the course of the measurements) would be sufficient to account for the discrepancy between the experiments and our calculations.

## **Acknowledgement**

The authors are grateful to Adam Willard, Amish Patel and Gil Nathanson for helpful discussions, and to Walter Drisdell, Ron Cohen and Richard Saykally for advice on many experiments devoted to this topic, including their own work, which motivated this current paper. In the early stages, P.V. was supported by a Berkeley Fellowship, then by NIH Grant No. R01-GM078102-04. D.C. was also supported by the Director, Office of Science, Office of Basic Energy Sciences, Materials Sciences and Engineering Division and Chemical Sciences, Geosciences, and Biosciences Divi-

sion of the U.S. Department of Energy under Contract No. DE-AC02-05CH11231. Both the raw evaporation trajectories and the source code for the programs used in the analysis are available upon request from the authors.

**Supporting Information Available:** Distribution of times at which trajectories leave basin  $A$  and enter basin  $B$ , which support using trajectories of length 3 ps. This material is available free of charge via the Internet at <http://pubs.acs.org>.

## Appendix

### Time reversibility and evaporation vs. condensation

The observables measured using TPS for evaporation can be related to those measured in simulations of condensation. Let  $h_A(x)$  and  $h_B(x)$  be indicator functions of basins  $A$  and  $B$ . They are equal to 1 if the phase space point  $x$  is in the respective basin, and 0 otherwise. The Boltzmann distribution, which specifies the initial conditions for our evaporation trajectories, is denoted by  $\rho(x)$ . The quantity  $P_T[x \rightarrow y]$  is the probability density that a trajectory of length  $T$  has its endpoint in the vicinity of  $y$ , given that it started at  $x$ . For the energy-conserving dynamics that we use in the text,

$$P_T[x \rightarrow y] = \delta[y - U_T(x)], \quad (13)$$

where  $U_T(x)$  is the time evolution operator over a time  $T$ .

The expectation of an observable  $\mathcal{G}$  measured at the endpoint  $b$  of an evaporation trajectory of the kind sampled by TPS is given by<sup>11</sup>

$$\langle \mathcal{G}(b) \rangle_{\text{evap}} = \frac{\int db \int da h_A(a) \rho(a) P_T[a \rightarrow b] h_B(b) \mathcal{G}(b)}{\int db \int da h_A(a) \rho(a) P_T[a \rightarrow b] h_B(b)}. \quad (14)$$

Conversely, the expectation of  $\mathcal{G}$  measured at the beginning point  $a$  of a condensation trajectory

can be defined as follows:

$$\langle \mathcal{G}(b) \rangle_{\text{cond}} = \frac{\int db h_B(b) \rho(b) \mathcal{G}(b)}{\int db h_B(b) \rho(b)}. \quad (15)$$

From these definitions, the following relation follows immediately:

$$\langle \mathcal{G}(b) \rangle_{\text{evap}} = \frac{\langle \mathcal{G}(b) \int da h_A(a) P_T[a \rightarrow b] \rangle_{\text{cond}}}{\langle \int da h_A(a) P_T[a \rightarrow b] \rangle_{\text{cond}}}. \quad (16)$$

Any configuration  $x$  can be mapped onto its time-reversed counterpart, which we denote  $\tilde{x}$ , by inverting the direction of all the particle momenta. For time-reversible dynamics, such as that used in the text, we have

$$P_T[a \rightarrow b] = P_T[\tilde{b} \rightarrow \tilde{a}], \quad (17)$$

and further, for energy-conserving dynamics, if  $a$  and  $b$  are in the same trajectory, then

$$\rho(a) = \rho(b). \quad (18)$$

With these relation, we can rewrite Eq. (16) in a more usable form,

$$\langle \mathcal{G}(b) \rangle_{\text{evap}} = \frac{\langle \mathcal{G}(b) \int da P_T[\tilde{b} \rightarrow \tilde{a}] h_A(a) \rangle_{\text{cond}}}{\langle \int da P_T[\tilde{b} \rightarrow \tilde{a}] h_A(a) \rangle_{\text{cond}}}, \quad (19)$$

$$= \frac{\langle \mathcal{G}(\tilde{b}) \int da P_T[b \rightarrow a] h_A(a) \rangle_{\text{cond}}}{\langle \int da P_T[b \rightarrow a] h_A(a) \rangle_{\text{cond}}}. \quad (20)$$

In the second equation, we have renamed the integration variables  $a$  and  $b$ , and exploited that  $h_A(a) = h_A(\tilde{a})$  and  $h_B(b) = h_B(\tilde{b})$ .

Equation (20) tells us that averages over TPS trajectories are equivalent to time-reversed averages over trajectories that start in B and end in basin A after time  $T$ . A priori, there is no requirement that the water that is condensing have an initial velocity that is directed towards the liquid slab, though trajectories that do not satisfy this condition are very unlikely to end in basin A.

A subtle point about Equation (20) is that the conditional factor  $\int da P_T[b \rightarrow a] h_A(a)$  cannot be approximated as  $1/2$  for large  $T$ . Indeed, basin B is potentially unbounded, so no matter how large



a  $T$  is chosen, there will be configurations in  $B$  with an initial velocity of the isolated water is too low for the system to escape basin  $B$  in time  $T$ . There are two potential solutions to this problem. One is to make basin  $B$  finite. Alternately, and more revealingly, one can model the consequence of the unboundedness of basin  $B$ , as we do below.

For concreteness, we consider a simpler definition of  $B$  than the one used in the text, which is easier to analyze and allows us to make the connection between the discussion here and kinetic rate theory.<sup>40</sup> Let  $z(b)$  be the  $z$ -coordinate of the evaporated water molecule's center of mass, and let  $v_z(b)$  be the corresponding component of the velocity. The simpler basin  $B$  consists of all configurations  $b$  for which  $z(b) > z^*$ . With this definition, we can make the following approximation:

$$P_T[b \rightarrow a]h_A(a) \approx \Theta[|v_z(b)|T - (z(b) - z^*)]P_\tau[b^* \rightarrow a], \quad (21)$$

with  $\tau \ll T$  a small, fixed time and  $b^*$  the point along the trajectory starting at  $b$  where  $z$  is first equal to  $z^*$ . In other words, the probability for a configuration  $b$  to end in basin  $A$  is mostly determined by whether  $T$  is long enough to get to the boundary of  $B$ , and then a kinetic factor that's virtually independent of  $T$ . We also assume that  $\mathcal{G}(b)$  is independent of  $z(b)$ , so we can replace  $\mathcal{G}(b)$  by  $\mathcal{G}(b^*)$ . Since the mapping from  $b$  to  $b^*$  is area preserving, we have

$$\langle \mathcal{G}(b) \rangle_{\text{evap}} \approx \frac{\langle \mathcal{G}(b^*) |v_z(b)| \delta[z(b) - z^*] \int da P_\tau[b \rightarrow a] h_A(a) \rangle_{\text{cond}}}{\langle |v_z(b)| \delta[z(b) - z^*] \int da P_\tau[b \rightarrow a] h_A(a) \rangle_{\text{cond}}}. \quad (22)$$

In comparison, the transmission coefficient for a reaction from  $B$  to  $A$  after a transient time  $\tau$  is given by<sup>40</sup>

$$\kappa_{B \rightarrow A}(\tau) = \frac{\langle |v_z(b)| \delta[z(b) - z^*] \int da P_\tau[b \rightarrow a] h_A(a) \rangle_{\text{cond}}}{\langle |v_z(b)| \delta[z(b) - z^*] \cdot (1/2) \rangle_{\text{cond}}}. \quad (23)$$

As is normal in reaction rate calculations, this transmission coefficient is almost independent of  $\tau$  for values of  $\tau$  greater than molecular timescales but smaller than implied by typical reaction rates. Here, those conditions require that  $1 \text{ ps} \ll \tau \ll 1 \text{ ns}$ . In this plateau regime, the transmission coefficient is equal to the uptake coefficient,  $\gamma$ . If this coefficient is 1 and  $z(b)$  is high enough that

an initially evaporating water molecule does not recondense, then we have

$$\int da P_{\tau}[b \rightarrow a] h_A(a) \approx \Theta[-v_z(b)], \quad (24)$$

so that

$$\langle \mathcal{G}(b) \rangle_{\text{evap}} \approx \frac{\langle \mathcal{G}(\tilde{b}) | v_z(b) | \delta[z(b) - z^*] \Theta[-v_z(b)] \rangle_{\text{cond}}}{\langle |v_z(b)| \delta[z(b) - z^*] \Theta[-v_z(b)] \rangle_{\text{cond}}}. \quad (25)$$

The quantity on the right-hand sides of Equations (22) and (25) is what is directly measured in condensation simulations. Obtaining them required several assumptions, all of which are reasonable in the context of this paper. However, our treatment here highlights the assumptions explicitly, and will be useful in contexts where these assumptions may not apply.

One simple application of Equations (22) and (25) is to calculate the distribution of  $v_z$  for the evaporated water molecules. Substituting  $\mathcal{G}(b) = \delta[v_z(b) - v_f]$  immediately yields Equation (9).

## Choice of density smoothing function $\phi(r)$

In the main text, the liquid-vapor interface is defined as an isosurface of the smoothed density field  $\tilde{\rho}(\mathbf{r})$ , constructed by convoluting the instantaneous water density (a sum of Dirac delta functions) with a smoothing kernel,  $\phi(r)$ . In Ref. 31, the choice for  $\phi(r)$  was a Gaussian of width  $\xi$ , truncated and shifted at  $r = 3\xi$ . Since our study focuses on the curvature of the liquid-vapor interface, the discontinuity in first and second derivatives of  $\phi(r)$  at the cutoff point is inconvenient. Instead, to ensure that  $\tilde{\rho}(\mathbf{r})$  is sufficiently smooth, we use a  $\phi(r)$  that results from stitching two cubic functions of  $r$  at the point  $r = c$ , subject to the following conditions: (a)  $\phi(r)$ ,  $\phi'(r)$  and  $\phi''(r)$  are continuous at  $r = c$ , (b)  $\phi(3\xi) = 0$ , (c)  $\phi'(0) = \phi'(3\xi) = 0$ , (d)  $\phi''(3\xi) = 0$ , (e)  $\int_0^\infty dr 4\pi r^2 \phi(r) = 1$ . These eight conditions uniquely specify  $\phi(r)$ . The stitching point is chosen empirically to be  $c = 2.1\xi$  so that  $\phi(r)$  closely resembles a Gaussian with standard deviation  $\xi$ . In Ref. 31, a value of  $\xi = 2.4 \text{ \AA}$  was chosen, which leads to about 7% of our trajectories having an ambiguous liquid-vapor interface at some timestep (i.e., Eq. (2) defining more than two liquid-vapor interfaces). We have found it convenient to use a slightly higher value,  $\xi = 2.5 \text{ \AA}$ , whereby the fraction of trajec-

tories with ambiguous liquid-vapor interfaces at any timestep drops to about 3%. For simplicity, all of these trajectories are discarded in their entirety in the analyses above.

## **Umbrella sampling with respect to the position of the liquid-vapor interface**

We have used umbrella sampling to collect statistics on rare configurations of our system where a probe water molecule is at a fixed perpendicular distance  $a$  (or  $a'$ ) from the instantaneous liquid-vapor interface. To do this, we have used the indirect umbrella sampling method (INDUS) that we have previously used in different contexts.<sup>41</sup> Briefly, we umbrella sample along a different coordinate that tracks  $a$ , use MBAR<sup>42</sup> to properly reweight all our samples, then compute histograms for  $a$  and possibly other variables from these weighted samples. The coordinate we use is the distance  $\tilde{a}$  from the probe water molecule to the instantaneous liquid-vapor interface directly below it. Let  $h(x, y; \mathbf{r}^N)$  be the  $z$ -coordinate of the liquid-vapor interface with the given values of  $x$  and  $y$ , which in turn depends on the positions of the  $N$  water oxygen atoms. The umbrella potential we use is

$$V(\mathbf{r}^N) = \frac{\kappa}{2} [z_n - h(x_n, y_n; \mathbf{r}^N) - \tilde{a}]^2. \quad (26)$$

Here,  $n$  is the index of the probe water molecule, with coordinates  $(x_n, y_n, z_n)$ . The value of  $h(x_n, y_n; \mathbf{r}^N)$  is defined implicitly by the equation

$$\tilde{\rho}(x_n, y_n, h(x_n, y_n; \mathbf{r}^N); \mathbf{r}^N) = (1/2)\rho_\ell. \quad (27)$$

We henceforth suppress the dependence of it on  $\mathbf{r}^N$ . In a slab of water, there are usually two disjoint interfaces at the slab's top and bottom, so this equation has two solutions. For concreteness, we always refer to the top interface of the slab.

To calculate  $h(x_n, y_n)$  quickly at every timestep, as well as its gradient with respect to particle positions, we note that the value of  $h(x_n, y_n)$  at one timestep is similar to its value at the next timestep. We have thus implemented a parallel Newton-Raphson solver to calculate  $h(x_n, y_n)$ , with the starting guess at one timestep equal to the value of  $h(x_n, y_n)$  at the previous timestep. In a

typical simulation, convergence to  $10^{-3} \text{ \AA}$  occurs after just one or two iterations.

To calculate the forces implied by the umbrella potential, we need to calculate the gradient of Equation (26) with respect to particle positions. We present explicit expression below, where  $h$  and its derivatives are evaluated at  $(x_n, y_n)$ , while  $\tilde{\rho}$  and its derivatives are evaluated at  $(x_n, y_n, h(x_n, y_n))$ . To simplify the calculation, we assume that the tagged particle  $n$  is not a water oxygen, and then relax this restriction. By taking the total derivative of Equation (27) with respect to the position of oxygen atom  $i$ , we find that

$$\frac{d(\tilde{\rho} - \rho_\ell/2)}{d\mathbf{r}_i} = \frac{\partial \tilde{\rho}}{\partial z} \frac{dh}{d\mathbf{r}_i} + \frac{\partial \tilde{\rho}}{\partial \mathbf{r}_i} = 0. \quad (28)$$

Hence,

$$\frac{dh}{d\mathbf{r}_i} = -\frac{\partial \tilde{\rho}}{\partial \mathbf{r}_i} / \frac{\partial \tilde{\rho}}{\partial z}. \quad (29)$$

The derivative with respect to the position of particle  $n$  is obtained similarly, so

$$\frac{d(\tilde{\rho} - \rho_\ell/2)}{dx_n} = \frac{\partial \tilde{\rho}}{\partial x} + \frac{\partial \tilde{\rho}}{\partial z} \frac{dh}{dx_n} = 0, \quad (30a)$$

$$\frac{d(\tilde{\rho} - \rho_\ell/2)}{dy_n} = \frac{\partial \tilde{\rho}}{\partial y} + \frac{\partial \tilde{\rho}}{\partial z} \frac{dh}{dy_n} = 0, \quad (30b)$$

$$\frac{d(\tilde{\rho} - \rho_\ell/2)}{dz_n} = 0. \quad (30c)$$

Hence,

$$\frac{dh}{dx_n} = -\frac{\partial \tilde{\rho}}{\partial x} / \frac{\partial \tilde{\rho}}{\partial z}, \quad (31a)$$

$$\frac{dh}{dy_n} = -\frac{\partial \tilde{\rho}}{\partial y} / \frac{\partial \tilde{\rho}}{\partial z}, \quad (31b)$$

$$\frac{dh}{dz_n} = 0. \quad (31c)$$

If the probe water molecule  $n$  is itself included in the definition of the liquid-vapor interface, then  $dh/d\mathbf{r}_n$  is the sum of the right-hand sides of Equations (29) and (31).

## Supplementary Information: Length of evaporation trajectories

In this section, we show that the 3 ps length of our TPS trajectories is long enough.

For each trajectory, let  $t_A$  be the latest time for which the system is in basin  $A$ , and let  $t_B$  be the latest time for which the system is not in basin  $B$ . These times roughly characterize the points along the trajectory at which the evaporation event begins and concludes. Figure 10 shows the distribution of the time difference  $t_B - t_A$ . Most evaporation events take under 1 ps, and very few take just under 3 ps. Hence, the 3 ps trajectory length we chose to use for our TPS sampling is long enough. Correcting the distribution of times  $t_B - t_A$  for the bias towards short evaporation events owing to their larger number of possible starting times does not change this conclusion. This is demonstrated in Figure 11, which shows the distributions of times  $t_B$ . If the TPS trajectory length is sufficiently long, then this distribution should rise from zero at small  $t_B$  and plateau to a constant for  $t_B$  much larger than the typical time for an  $A$ -to- $B$  transition to occur. This is indeed observed. Were the TPS trajectory length too short, there would be no plateau region.

### References

- (1) Kolb, C. E. et al. *Atmos. Chem. Phys.* **2010**, *10*, 10561–10605.
- (2) Eames, I. W.; Marr, N. J.; Sabir, H. *Int. J. Heat Mass Tran.* **1997**, *40*, 2963–2973.
- (3) Drisdell, W. S.; Saykally, R. J.; Cohen, R. C. *J. Phys. Chem. C* **2010**, *114*, 11880–11885.
- (4) Li, Y. Q.; Davidovits, P.; Kolb, C. E.; Worsnop, D. R. *J. Phys. Chem. A* **2001**, *105*, 10627–10634.
- (5) Zientara, M.; Jakubczyk, D.; Kolwas, K.; Kolwas, M. *J. Phys. Chem. A* **2008**, *112*, 5152–8.
- (6) Winkler, P.; Vrtala, A.; Wagner, P.; Kulmala, M.; Lehtinen, K.; Vesala, T. *Phys. Rev. Lett.* **2004**, *93*.

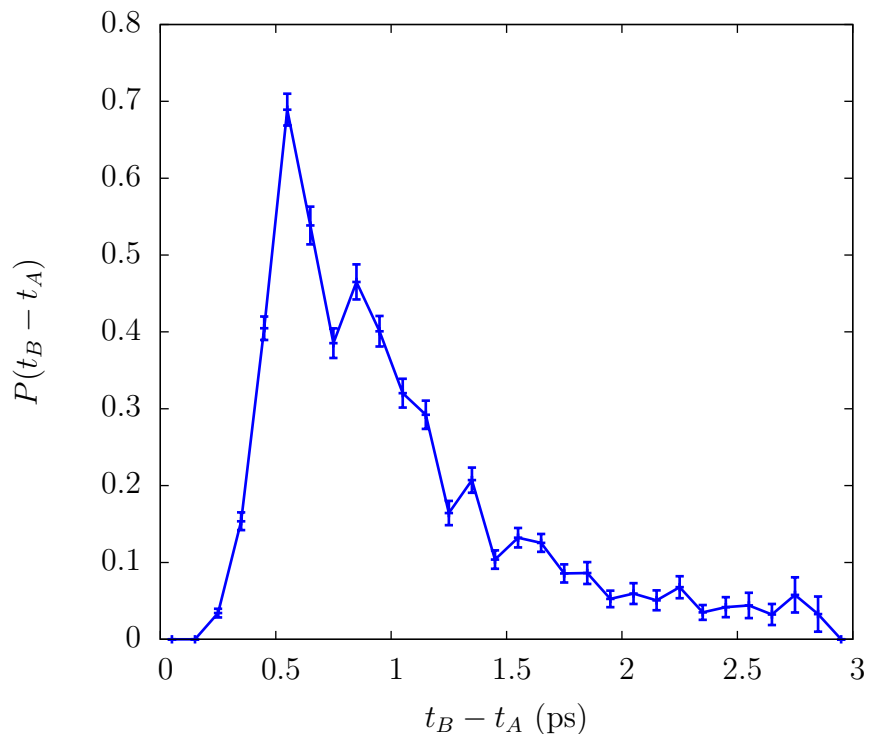


Figure 10: Distribution of evaporation event durations.

- (7) Winkler, P. M.; Vrtala, A.; Rudolf, R.; Wagner, P. E.; Riipinen, I.; Vesala, T.; Lehtinen, K. E. J.; Viisanen, Y.; Kulmala, M. *J. Geophys. Res.* **2006**, *111*, D19202.
- (8) Smith, J. D.; Cappa, C. D.; Drisdell, W. S.; Cohen, R. C.; Saykally, R. J. *J. Am. Chem. Soc.* **2006**, *128*, 12892–12898.
- (9) Drisdell, W. S.; Cappa, C. D.; Smith, J. D.; Saykally, R. J.; Cohen, R. C. *Atmos. Chem. Phys.* **2008**, *8*, 6699–6706.
- (10) Drisdell, W. S.; Saykally, R. J.; Cohen, R. C. *P. Natl. Acad. Sci. U.S.A.* **2009**, *106*, 18897–18901.
- (11) Bolhuis, P. G.; Chandler, D.; Dellago, C.; Geissler, P. L. *Annu. Rev. Phys. Chem.* **2002**, *53*, 291–318.
- (12) Mason, P. E. *J. Phys. Chem. A* **2011**, *115*, 6054–6058.

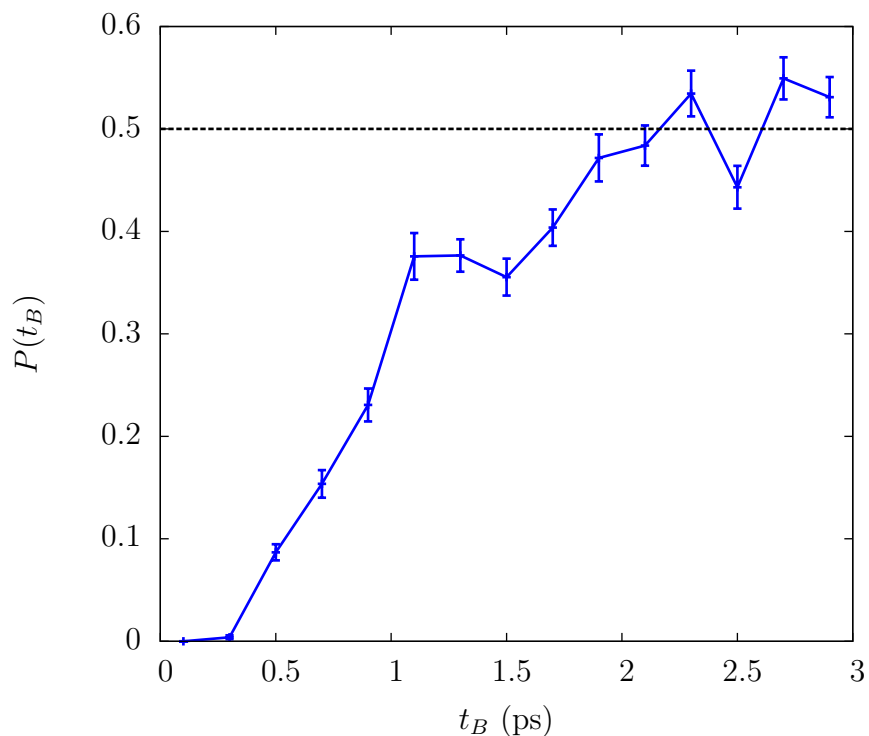


Figure 11: Distribution of times at which the evaporation event completes.

- (13) Tsuruta, T.; Nagayama, G. *J. Phys. Chem. B* **2004**, *108*, 1736–1743.
- (14) Morita, A.; Sugiyama, M.; Kameda, H.; Koda, S.; Hanson, D. R. *J. Phys. Chem. B* **2004**, *108*, 9111–9120.
- (15) Viececi, J.; Roeselová, M.; Tobias, D. *J. Chem. Phys. Lett.* **2004**, *393*, 249–255.
- (16) Plimpton, S. *J. Comp. Phys.* **1995**, *117*, 1–19.
- (17) Berendsen, H. J. C.; Grigera, J. R.; Straatsma, T. P. *J. Phys. Chem.* **1987**, *91*, 6269–6271.
- (18) Hockney, R.; Eastwood, J. *Computer Simulation Using Particles*; Taylor & Francis, 1988; p 540.
- (19) Miyamoto, S.; Kollman, P. A. *J. Comput. Chem.* **1992**, *13*, 952–962.
- (20) Mark, P.; Nilsson, L. *J. Phys. Chem. A* **2001**, *105*, 9954–9960.

- (21) Vega, C.; McBride, C.; Sanz, E.; Abascal, J. L. F. *Phys. Chem. Chem. Phys.* **2005**, *7*, 1450–1456.
- (22) Motakabbir, K. A.; Berkowitz, M. L. *J. Phys. Chem. B* **1990**, *94*, 8359–8362.
- (23) Aragonés, J. L.; MacDowell, L. G.; Vega, C. *J. Phys. Chem. A* **2011**, *115*, 5745–58.
- (24) Huang, D. M.; Geissler, P. L.; Chandler, D. *J. Phys. Chem. B* **2001**, *105*, 6704–6709.
- (25) Vega, C.; de Miguel, E. *J. Chem. Phys.* **2007**, *126*, 154707.
- (26) Patel, A. J.; Varilly, P.; Chandler, D.; Garde, S. *J. Stat. Phys.* **2011**, *145*, 265–275.
- (27) Errington, J. R.; Panagiotopoulos, A. Z. *J. Phys. Chem. B* **1998**, *102*, 7470–7475.
- (28) Luzar, A.; Chandler, D. *Nature* **1996**, *379*, 55–57.
- (29) Geissler, P. L.; Dellago, C.; Chandler, D. *J. Phys. Chem. B* **1999**, *103*, 3706–3710.
- (30) Geissler, P. L.; Chandler, D. *J. Chem. Phys.* **2000**, *113*, 9759–9765.
- (31) Willard, A. P.; Chandler, D. *J. Phys. Chem. B* **2010**, *114*, 1954–1958.
- (32) Chandler, D. *Introduction to Modern Statistical Mechanics*; OUP USA, 1987; p 256.
- (33) Kreyszig, E. *Differential Geometry (Dover Books on Mathematics)*; Dover Publications Inc., 1991; p 366.
- (34) Takahama, S.; Russell, L. M. *J. Geophys. Res.-Atmos.* **2011**, *116*, D02203.
- (35) Vácha, R.; Slavíček, P.; Mucha, M.; Finlayson-Pitts, B. J.; Jungwirth, P. *J. Phys. Chem. A* **2004**, *108*, 11573–11579.
- (36) Dang, L. X.; Garrett, B. C. *Chem. Phys. Lett.* **2004**, *385*, 309–313.
- (37) Miller, W. H. *J. Chem. Phys.* **2012**, *136*, 210901.



- (38) Craig, I. R.; Manolopoulos, D. E. *J. Chem. Phys.* **2004**, *121*, 3368–73.
- (39) Suzuki, H.; Matsuzaki, Y.; Muraoka, A.; Tachikawa, M. *J. Chem. Phys.* **2012**, *136*, 234508.
- (40) Chandler, D. *J. Chem. Phys.* **1978**, *68*, 2959.
- (41) Patel, A. J.; Varilly, P.; Jamadagni, S. N.; Acharya, H.; Garde, S.; Chandler, D. *P. Natl. Acad. Sci. U.S.A.* **2011**, *108*, 17678–17683.
- (42) Shirts, M. R.; Chodera, J. D. *J. Chem. Phys.* **2008**, *129*, 124105.